Boosting fast ignition heating through interaction between ultrahigh-contrast heating lasers and a cone-shaped target

Ryunosuke Takizawa,[1,2,*] Alessio Morace,[1] Yuki Abe,[3,1] Yasunobu Arikawa,[1] Baojun Zhu,[1] Hiroki Morita,[4,1] Zechen Lan,[1] Jinyuan Dun,[1,2] Takumi Tsuido,[1,2] Yuga Karaki,[1,2] Hiroki Matsubara,[1,2] King Fai Farley Law,[1] Chang Liu,[1,5] Kazuki Matsuo,[1] Akifumi Yogo,[1] Akifumi Iwamoto,[6] Hideo Nagatomo,[1] Tomoyuki Johzaki,[7,1] Mitsuo Nakai,[1] Hiroyuki Shiraga,[1] Ryosuke Kodama,[3,1] Yasuhiko Sentoku,[1] and Shinsuke Fujioka[1,6,†]

[1]*Institute of Laser Engineering, The University of Osaka, 2-6 Yamada-Oka, Suita, Osaka 565-0871, Japan*
[2]*Department of Physics, Graduate School of Science, The University of Osaka, Toyonaka 560-0043, Japan*
[3]*Graduate School of Engineering, The University of Osaka, 2-1 Yamada-Oka, Suita, Osaka 565-0871, Japan*
[4]*Faculty of Engineering, Utsunomiya University, 7-1-2 Yoto, Utsunomiya, Tochigi 321-8585, Japan*
[5]*National Institutes for Quantum and Radiological Science and Technology, 8-1-7 Umemidai, Kizugawa-shi, Kyoto 619-0215, Japan*
[6]*National Institute for Fusion Science, 322-6 Oroshi, Toki, Gifu 509-5292, Japan*
[7]*Graduate School of Advanced Science and Engineering, Hiroshima University, 1-4-1 Kagamiyama, Higashi-Hiroshima, Hiroshima 739-8527, Japan*

(Received 5 November 2024; accepted 31 January 2025; published 24 April 2025)

In pursuing a carbon-neutral society, inertial fusion energy is a pivotal technology, offering a sustainable and virtually limitless energy source. Enhancing plasma heating efficiency is crucial for inertial fusion energy, following the ignition success using the laser-indirect-drive central-ignition approach at the U.S. National Ignition Facility. Fast ignition is a potentially high-efficiency approach among inertial confinement fusion methods. However, it remains significantly challenging due to the large divergence angle of relativistic electron beams (REBs) produced by high-intensity laser pulses. Here, we demonstrate the spontaneous collimation of REBs facilitated by an ultrahigh contrast of the heating laser in conjunction with a cone-shaped target. This collimation doubles the plasma heating efficiency compared to that achieved with the lower-contrast laser, as conducted with LFEX laser at Osaka University. This finding enables the use of a larger spot laser under ignition conditions, which is crucial for achieving the heating efficiency required for fusion ignition by reducing laser intensity and the mean kinetic energy of REBs. This collimation method significantly advances the field of inertial confinement fusion, elevating fast ignition to a practical level.

DOI: 10.1103/PhysRevResearch.7.023081

I. INTRODUCTION

Recent achievements at the National Ignition Facility in the U.S. indicate that the feasibility of nearly limitless energy production through inertial confinement fusion (ICF) is becoming apparent. The generalized Lawson criteria exceeded unity using the laser-indirect-drive central-ignition approach of ICF [1–3], and ignition was achieved in 2022 [4]. The produced nuclear fusion energy was equivalent to 190% of the injected laser energy (target gain of 1.9). A target gain of 100 is a goal to realize inertial fusion energy (IFE) [5] considering the entire energy flow of the IFE system with the assumptions of laser-driver efficiency (5%) and recycling power fraction (25%). The conveyance of laser energy to the fuel is critical for ICF because the target gain is positively correlated with the internal energy of a fuel. However, energy coupling from the laser to the hot spot was about 0.6% [2] in the above ignition experiments [1–3]. An improvement in energy coupling is required for the realization of IFE.

Fast ignition [6] (FI), which instantaneously heats a dense plasma core by injecting energy from the outside, is expected to be an efficient ignition approach. Plasma heating with a relativistic electron beam (REB) accelerated by a short-pulse laser having a relativistic intensity ($I_L\lambda_L^2 > 1.37 \times 10^{18}$, where I_L and λ_L are respectively the intensity in W/cm^2 and the wavelength in μm of the laser) is divided into three major mechanisms [7], namely drag heating, resistive heating, and diffusive heating. Our experimental work focuses on drag heating, which is collisional heating between relativistic electrons (REs), ions and bulk electrons in the fuel. Here, the drag heating efficiency η is simplified as follows:

$$\eta = \eta_{\mathrm{REB}}\eta_{\mathrm{col}}\eta_{\mathrm{dep}},$$

$$\eta_{\mathrm{REB}} = \frac{(\text{sum of REB kinetic energy})}{(\text{incident laser energy})},$$

$$\eta_{\mathrm{col}} = \frac{(\text{REB energy injected to fuel core})}{(\text{sum of REB kinetic energy})},$$

$$\eta_{\mathrm{dep}} = \frac{(\text{REB energy deposit in fuel core})}{(\text{REB energy injected to fuel core})}.$$

*Contact author: takizawa.ryunosuke.ile@osaka-u.ac.jp
†Contact author: fujioka.shinsuke.ile@osaka-u.ac.jp

When a heating laser is injected into an underdense plasma, the heating efficiency significantly decreases due to the following three effects. First, development of Weibel or other beam-plasma instabilities generates a spatially extended and turbulent strong magnetic field in a long-scale-length plasma, and the turbulent magnetic field scatters REs and decreases $\eta_{\rm col}$. The local electron angular distribution $f(r,\theta)$ [8] at the radial position of laser beam r is represented using the dispersion angle $\Delta\theta$ and the local electron mean propagation angle called deviation angle $\theta_r(r)$ as

$$f(r,\theta) \propto \exp\left[-\frac{(\theta-\theta_r(r))^2}{\Delta\theta_0^2}\right]. \quad (1)$$

The dispersion angle depends on the laser intensity and not on the plasma scale length [9,10]. The deviation angle depends on the scattering magnetic fields formed in the plasma, and thus, it depends on the plasma scale length [8]. Second, the acceleration mechanism of REs in plasma is enhanced [11–14], leading to the high energy of REBs [15,16] and a decrease in $\eta_{\rm dep}$. The range of REBs in plasma is approximated as $\mathcal{R}({\rm g/cm^2}) \sim 0.6\langle E_{\rm REB}\rangle$ [17], where $\langle E_{\rm REB}\rangle$ is the mean kinetic energy of the REB in MeV. The range should be comparable to the areal density of the hot spot (0.3–0.6 g/cm^2) for efficient heating. The generation of an excessively energetic REB, whose mean kinetic energy is larger than the ponderomotive scaling, has been observed in multi-picosecond kilojoule laser facilities [18,19]. Third, the generation points of REs move further away from the fuel core, resulting in a reduction of RE energy before they reach the fuel. Hence, the efficacy of a target with a cone attached to the fuel has been proposed by Norreys *et al.* [20] and experimentally demonstrated by Kodama *et al.* [21] to prevent the inflow of the ablation plasma formed during fuel compression towards the laser-plasma interaction region. Additionally, these three effects are caused not only by the plasma formed during fuel compression but also by the pre-plasma formed by the heating laser itself. Previous experiments have shown that preceding pulses and a pre-plasma negatively affect plasma heating [22–28].

Here, we revealed the spontaneous collimation of the REB by combining the ultrahigh-contrast heating laser with a cone target; therefore, the efficiency of the compressed plasma heating increased. When the high-contrast laser travels into the cone, the peripheral region of the laser spot reaches the cone tip surface after being reflected inwardly at the cone wall. As a result, the Poynting vector at the cone tip surface is directed towards the laser's central axis, and then the average momentum of the REs generated at the cone tip surface is directed towards the central axis of the laser beam. Namely, the deviation angle acts to suppress the dispersion angle. This phenomenon is clearly described in Fig. 1 calculated with the particle-in-cell simulation SMILEI [29]. The magenta arrows represent the average Poynting vector, and the white arrows represent the average momentum of REs. The average Poynting vector and the average momentum of REs at the cone tip surface are directed towards the laser's central axis. Consequently, the REB is collimated. This phenomenon only appears in high-contrast lasers because the laser does not efficiently reflect at the inner wall of the cone when preplasma is present on the wall. The simulation parameters are described in the Appendix.

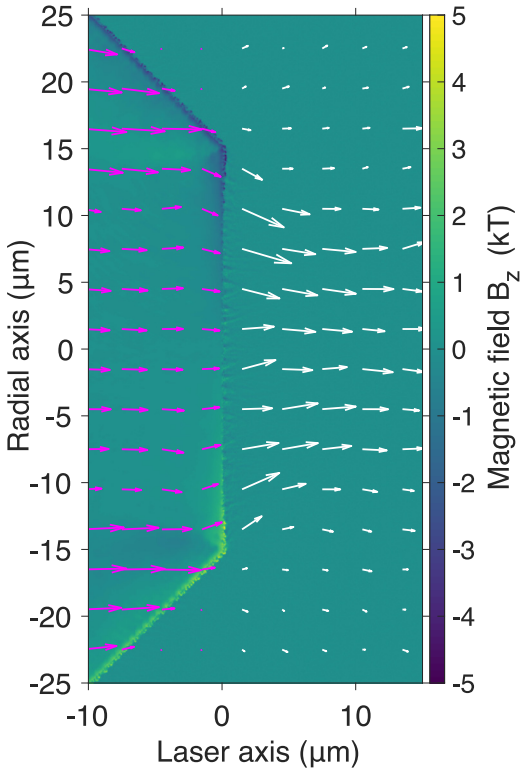

FIG. 1. REB collimation in a particle-in-cell simulation. The Poynting vectors (magenta arrows) at the cone tip surface make the mean momentum of REs (white arrows) flow to the central axis of the laser. The color map shows Z components of **B** fields directed into the paper.

A plasma mirror (PM) made from transparent glass with an antireflection coating [30–34] was used to improve the laser contrast. The preceding pulses pass through the PM because their intensities are below the plasma formation threshold (typically 6–7 J/cm^2) on the PM [34]. Then, the intensity of preceding pulses is reduced. When the laser intensity of the preceding pulse or the main pulse exceeds the plasma formation threshold on the PM, plasma forms on the surface of the PM and reflects subsequent laser light toward the target. The performance of the antireflection coating and the original pulse contrast determines the contrast of the laser reflected by the PM. The experiment was conducted on the LFEX laser at Osaka University. The pulse duration, typical energy per beam, wavelength, and F-number were 1.3 ps, 300 J/beam, 1.053 μm, and 10, respectively. The PM was concave fused silica glass with a transmittance of 99.8% at 1.053 μm in this study. The curvature radius and diameter of the PM were 203.2 and 50.8 mm, respectively. The PM was positioned 203.2 mm downstream from the first focal point and formed an image of the first focal spot at the tip of the cone with an image magnification of 1. Figure 2 represents the waveform of LFEX, where the red curve indicates the low-contrast case under normal conditions, the blue curve is the medium-contrast case achieved through the fine tuning of the laser, and the black curve is the high-contrast case achieved by using a PM

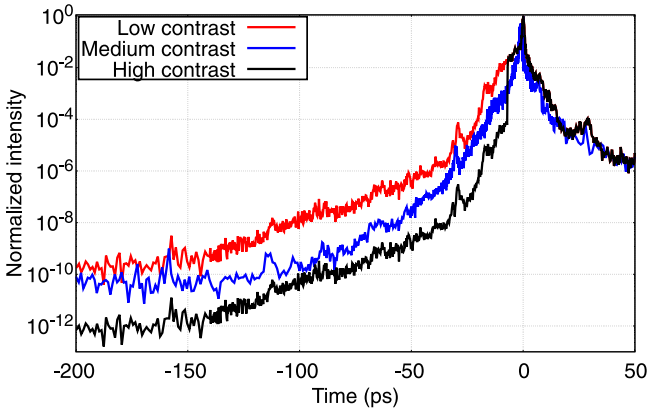

FIG. 2. Temporal shape of normalized laser intensity. The low-contrast case (red curve) is the usual contrast for the LFEX laser. The medium-contrast case (blue curve) has contrast improved without a PM. The high-contrast case (black curve) is reflected by adding a PM to the low-contrast case. The black curve was calculated from the red curve using the reflectivity of the PM (45%) and the transmittance of the antireflective coating (99.8%) of the PM.

in the low-contrast case. In some cases, laser amplification may be saturated at the peak of the laser pulse while the preceding pulses are normally amplified; this results in worse contrast. We have obtained the middle contrast by turning the amplification condition just below the saturation threshold. The high-contrast case is calculated from the low-contrast case and follows the measured reflectivity depending on the laser flux on the PM. The reflectance of the PM was 0.2% until the laser intensity reached the plasma generation threshold, which was about 6^{+1}_{-2} ps before the laser peak in this study. After that, the reflectivity was $44 \pm 1\%$ [35].

II. EXPERIMENTAL OBSERVATION OF REB COLLIMATION WITH HIGH-CONTRAST HEATING LASER

We experimentally demonstrated the collimation of a REB by combining the high-contrast laser and the 100 μm tip cone target. The propagation of a REB through the tracer target [Fig. 3(a)], which was made of Cu(II) oleate [$Cu(C_{17}H_{33}COO)_2$], was measured. Cu-K_α lines were emitted when REs collided with the Cu atoms in the tracer target; thus, Cu-K_α represents the REB shape. The thickness, inner angle, and length of the gold cone were 7 μm, 45°, and 300 μm, respectively. A Ta block was attached to prevent the reflux of REs. The laser energy, pulse width, and laser intensity on the target for this shot were 300 ± 50 J, 1.6 ps, and $(2.4 \pm 0.4) \times 10^{18}$ W/cm^2, respectively. The mean kinetic energy of REB is 1.8 ± 0.2 MeV which is several times higher than the ponderomotive scaling in this shot. We have considered the high energy electrons comes from some electron acceleration mechanism caused by oblique laser irradiation on the cone side wall. Because the mean energy of REB with a planer target in the high-contrast case is about hundred keV, which is close to the ponderomotive value.

Figure 3(b) shows the two-dimensional emission density cross section of the Cu-K_α lines derived from the measured Cu-K_α emission image under the assumption of cylindrical symmetry along the heating laser axis. The gold cone was located at the bottom, as shown in Fig. 3(a). The full width at half maximum (FWHM) of the REB profile near the laser

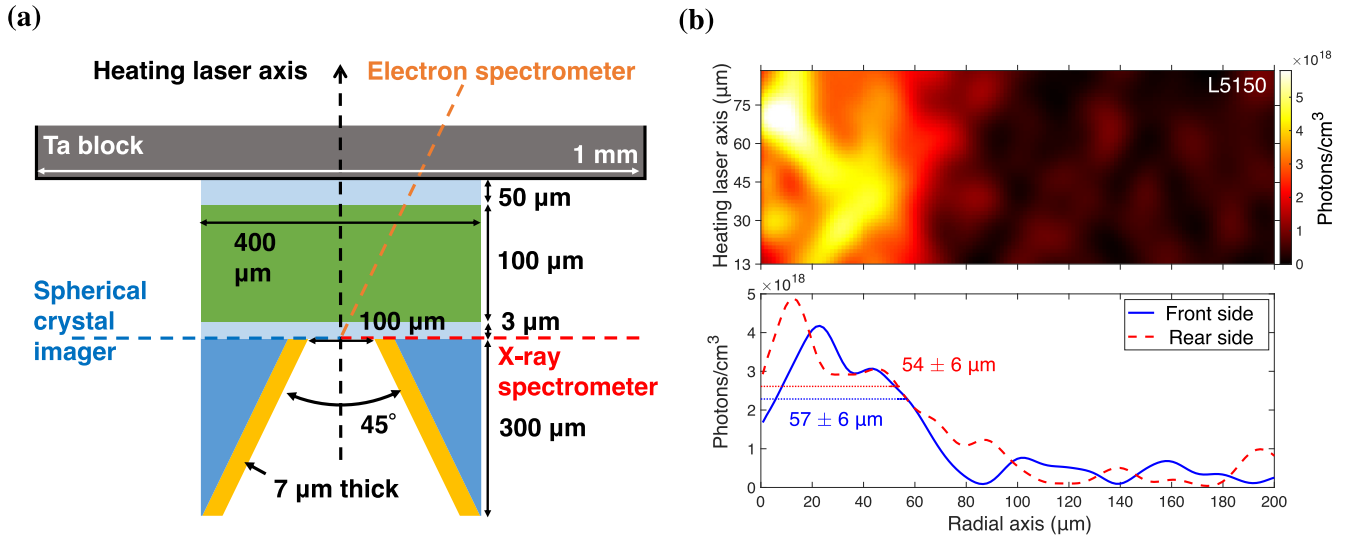

FIG. 3. (a) REB collimation measurement target. The tracer target was a 100-μm-thick plate of Cu(II) oleate [$Cu(C_{17}H_{33}COO)_2$] sandwiched between polystyrene sheets 3 μm and 50 μm thick. A gold cone, whose thickness, inner tip diameter, inner angle, and length were 7 μm, 100 μm, 45°, and 300 μm, respectively, was attached to the plate. The cone was buried in a polyvinyl alcohol block to simulate an ablation plasma. A Ta block was attached to the rear side of the tracer to prevent the reflux of REs. (b) Emission density cross section. The top figure shows the emission density cross section of the Cu-K_α lines. The heating laser was injected from the bottom, similar to the setup in panel (a). The heating axis is defined as the distance from the focal spot. The emission density is similar to the electron number density of an REB under the assumption that the energy distribution is the same in the emission region. The bottom figure shows the radial profile of the emission density averaged over a width of 5 μm on each of the front and rear surfaces.

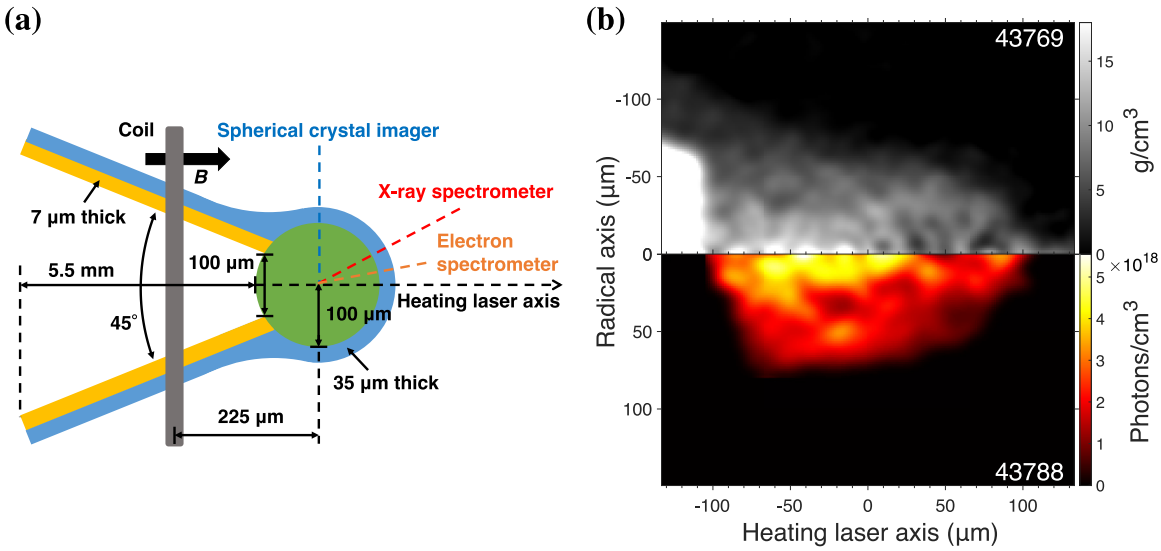

FIG. 4. (a) Experimental setup for heating experiment. The fuel surrogate was a solid sphere of Cu(II) oleate with a diameter of 200 μm compressed by six terawatt lasers (energy: 240 J/beam; wavelength: 0.526 μm) arranged with quasi-cylindrical symmetry. A gold cone, whose thickness, inner tip diameter, inner angle, and length were 7 μm, 100 μm, 45°, and 5.5 mm, respectively, was attached to the sphere. A polyvinyl alcohol coating with a thickness of 35^{+5}_{-0} μm was applied to both the solid sphere and the gold cone. The laser-driven coil used to generate a magnetic field was irradiated by three terawatt lasers (energy: 600 J/beam; wavelength: 1.053 μm). The laser-driven coil was placed 225 μm away from the center of the fuel. The magnetic field was generated along the heating laser axis. (b) (Top) Density cross section. The transmittance image measured using x-ray backlighting was converted into a mass density cross section using the inverse Abel transform. The cone was placed on the left side of the image (shot ID: 43769). (b) (Bottom) Cu-K_α emission density cross section. The Cu-K_α emission image measured by the spherical crystal imager was converted to an emission density cross section by assuming cylindrical symmetry and accounting for the opacity of the plasma. The photon densities were corrected by the absolute photon number of the Cu-K_α lines (shot ID: 43788).

interaction region (blue curve in Fig. 3) and at the backside (red dashed curve in Fig. 3) are 114 ± 13 μm and 108 ± 13 μm, respectively. A spherical crystal imager with a quartz (2131) crystal, whose radius of curvature was 200 mm and spatial resolution was 13 ± 5 μm (FWHM), was used for measuring the monochromatic images of the Cu-K_α lines. The images were spatially smoothed by a Gaussian filter with FWHM of 10 μm for reducing the speckle noise. The REB waist at the position where the REB propagates 120 μm from the cone tip was 200 μm, as determined by a previous study [36] that used a similar target shape in the low-contrast case. The divergence angle of the REB was significantly reduced by improving the contrast of the heating laser.

III. CONFIGURATION OF HEATING EXPERIMENT

We experimentally demonstrated that combining a high-contrast heating laser with a fuel surrogate having an attached cone leads to an increase in plasma heating efficiency due to the REB collimation. A cone-equipped solid sphere of Cu(II) oleate [37] with a diameter of 200 μm was used as the fuel surrogate [Fig. 4(a)]. The deposited energy of drag heating was evaluated based on the absolute photon number of the Cu-K_α lines emitted when electrons collided with Cu atoms in the fuel surrogate, which caused inner-shell ionization with a certain probability. The correlation factor ($\sim 5 \times 10^{11}$ J photons^{-1} sr^{-1}) between the deposited energy and the absolute photon number of the Cu-K_α lines was calculated from electron-impact K-shell ionization cross-section models [38,39] and the stopping power model of electrons in high-density plasma [40] based on previous research [41,42]. The REB energy profiles for each shot, an average density of $\rho = 6.8$ g/cm^3, and an areal density of $\rho L = 0.14$ g/cm^2 within a diameter of 100 μm along the heating laser axis were used in this calculation. Figure 4(b) shows the measured plasma mass density and the emission cross section of Cu-K_α lines. The transmittance of the Cu-K_α lines through the plasma was evaluated using the Cu-K_α emission profile and the plasma's mass density profile. The absolute photon number of the measured Cu-K_α lines divided by the transmittance was used to evaluate the deposited energy. The heating efficiency is defined as the deposited energy, as evaluated from the correlation factor and the absolute photon number of the Cu-K_α lines, divided by the laser energy on the target. The method mentioned above can evaluate only the drag heating efficiency, not the resistive and diffusive heating. The resistive heating is caused by the collisional slow return current, which flows to maintain plasma current neutrality for the fast electron current. The return current ohmically heats bulk electrons; therefore, Cu-K_α emission is not related to the resistive heating. The diffusive heat transport is driven by the temperature gradient generated by drag heating and resistive heating. Cu-K_α is not emitted during the diffusive process. Hence, there is no correlation between Cu-K_α and diffusive heating efficiency.

Six beams of the GEKKO-XII laser at the Institute of Laser Engineering, Osaka University, were used for compressing the solid sphere in the heating experiment. The beams were arranged in a quasi-cylindrical geometry, where the symmetry axis corresponded to the heating laser axis. The pulse shape,

pulse duration, typical energy, wavelength, and F-number of the focus were Gaussian, 1.3 ns (FWHM), 240 J/beam, 0.526 μm, and 3, respectively. The focus positions of the six beams were set 375 μm behind the sphere center to enhance the laser irradiation uniformity on the spherical surface.

An external magnetic field was applied to the plasma in several shots for converging the REB [42]. A laser-driven coil [43] was used to converge the REB and increase heating efficiency [42]. The laser-driven coil consisted of two plates and an attached coil. It has been experimentally demonstrated that the laser-driven coil can generate a magnetic field of several hundred tesla [44] and focus the REB [42,45]. The laser-driven coil was irradiated by three beams of the GEKKO-XII laser. The energy and wavelength were 600 J/beam and 1.053 μm, respectively. The shape of the laser-driven coil used in this experiment was the same as that used in previous studies [42]. A magnetic field of 610 ± 30 T was generated 1 ns after the laser peak [44] under the same laser conditions. The coil was placed 225 μm from the center of the solid sphere to make the magnetic fields parallel to the heating laser. The magnetic field applied from the outside penetrated the gold cone [46]. In this paper, the magnetic field strength is assumed to be 600 T for all corresponding shots. Measuring the magnetic field for all shots is challenging owing to the harsh electromagnetic noise generated by the high-intensity heating laser and plasma interaction. We note that this assumption does not affect the conclusion and analysis of this work.

IV. ENHANCED HEATING EFFICIENCY THROUGH REB COLLIMATION

Due to the significant reduction of the REB divergence, the path length of REs traveling in the compressed plasma increased, which in turn led to an increase in the heating efficiency by improving the contrast of the heating laser. The increase in heating efficiency due to external magnetic fields was not observed in the high-contrast case, because the REB had already become collimated. In contrast, heating efficiency increased with the external magnetic field in the medium-contrast case. To understand the experimental results depending on multiple parameters, we have calculated the correlation coefficient, a statistical measure that describes the strength and direction of the relationship between heating efficiency and another parameter. A correlation factor of 1 indicates a perfect positive correlation, meaning that as one variable increases, the other also increases. A value of -1 indicates a perfect negative correlation, meaning that as one variable increases, the other decreases. A value of 0 indicates no correlation, implying that the variables are independent of each other. The correlation coefficient between heating efficiency and the presence or absence of an external magnetic field (1 or 0) was 0.13 for the high-contrast case and 0.79 for the medium-contrast case. The average drag heating efficiency of the compressed plasma increased 3.9-fold, from $1.3 \pm 0.3\%$ in the medium-contrast case to $5.1 \pm 1.0\%$ in the high-contrast case without the external magnetic field. Additionally, the partial correlation coefficients for heating efficiency across all data are as follows: contrast (high-contrast: 3, medium-contrast: 2, low-contrast: (1) is 0.88, heating timing is 0.49, and other parameters such as pulse width and laser energy have absolute values less than 0.36. The complete data table is provided in the Appendix (Tables I and II).

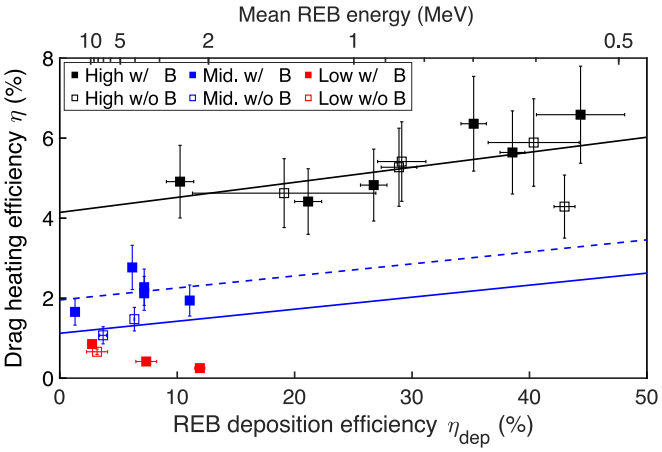

FIG. 5. Drag heating efficiency versus REB deposition efficiency. The heating efficiency was enhanced by improving the laser contrast. A difference of heating efficiencies between the high-contrast case with the **B** field (black filled squares) and the high-contrast case without the **B** field (black open squares) was not observed, because the REB had already been collimated.

The mean kinetic energy of the REB decreased with increasing pulse contrast. The average mean kinetic energy of the REB within the laser intensity of $(4–6) \times 10^{18}$ W/cm^2 was 1.4 MeV in the high-contrast case, 3.9 MeV in the medium-contrast case, and 9.4 MeV in the low-contrast case. However, the increase in heating efficiency, η, due to the rise in the energy deposition efficiency, η_{dep}, caused by the reduction in the mean kinetic energy of REB, was modest. Figure 5 shows η in relation to η_{dep}. Here, η_{dep} was calculated with the energy distribution of the REB and the stopping power model of electrons in high-density plasma [40]. The proportionality coefficient between η and η_{dep} is only 0.03–0.04. This indicates that the conversion efficiency from lasers to the REB, η_{REB}, decreased as the mean kinetic energy of the REB decreased because η_{col} is not substantially changed in the same laser contrast. In other words, the decrease in mean kinetic energy can be seen as a reduction in high-energy electrons. Indeed, prior research indicates that a decrease in the plasma scale length reduces the laser absorption fraction [47].

V. REALIZING THE PATH TO IGNITION: PRACTICAL PROSPECTS

The spontaneous REB collimation found in this study advances the FI approach to a practical implementation level. The current inefficiency in the FI approach arises from the inherent trade-off between the collisional efficiency, η_{col}, and the energy deposition efficiency, η_{dep}. The REB should be generated as close to the fuel as possible and the REB diameter at the generation point, which is comparable to the laser spot diameter, should be as small as possible for increasing collisional fraction η_{col}. Conversely, as the laser spot size is reduced, the laser intensity and the mean kinetic energy of the

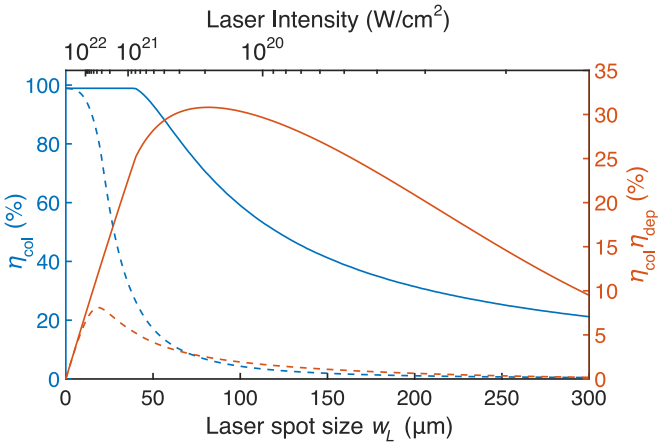

FIG. 6. Optimal laser spot size. The blue and orange curves describe $\eta_{\rm col}$ and $\eta_{\rm col}\eta_{\rm dep}$, respectively, for the previous situation (dashed curves) and REB collimation (solid curves). The REs generated at each laser-plasma interaction point can be directed toward the center of the plasma core in the collimation method, and then $\eta_{\rm col}$ decreases gradually.

REB increase and $\eta_{\rm dep}$ decreases. Therefore optimizing the laser spot size that maximizes $\eta_{\rm col}\eta_{\rm dep}$ is essential.

Using the electron stopping power model [40], the energy transfer efficiency from a REB to an ignition scale fuel core was calculated with the following assumption: REB has a three-dimensional spatial distribution, and the electrons move along straight lines in the plasma. The ignition-scale fuel core is assumed to have radius $R_{\rm core} = 20$ μm and density $\rho_{\rm core} = 300$ g/cm^3, and to be surrounded by a plasma with density $\rho_{\rm back} = 10$ g/cm^3. The energy, wavelength, and pulse duration of the heating laser in the ignition condition is set to $E_{\rm L} = 200$ kJ, $\lambda_{\rm L} = 0.351$ μm, and $\tau = 20$ ps, respectively. The distance from the fuel core center to the REB generation area is defined as $D = \max(w_{\rm L},\ R_{\rm core})$, where $w_{\rm L}$ is the laser spot diameter. The REB propagation is described in Eq. (1) with $\theta_r(r) = 0$ and $\Delta\theta = 40^\circ$, whose dispersion angle corresponds to a laser intensity of $I_{\rm L} \sim 10^{20}$ W/cm^2 [10]. The energy distribution of the REB is a Boltzmann distribution with mean energy that is calculated by ponderomotive scaling. Here, in the case of a high-contrast heating laser (collimated situation), the average momentum of the REs generated at each laser-plasma interaction point can be directed toward the center of the plasma core, increasing $\eta_{\rm col}$ by combining a high-contrast heating laser with an optimally shaped cone. In other words, the average momentum of the generated electrons is directed toward the center of the plasma core in the collimated situation (solid curves), while it is oriented along the laser axis in the noncollimated situation (dashed curves).

Figure 6 shows $\eta_{\rm col}$ (blue curves) and $\eta_{\rm col}\eta_{\rm dep}$ (red curves) for a 20 μm-diameter plasma core under the collimated situation (solid curves) and the noncollimated situation (dashed curves). As the laser spot expands, $\eta_{\rm col}$ decreases rapidly in the previous situation. For instance, at $w_{\rm L} = 100$ μm, $\eta_{\rm col}$ is reduced to 1%. The peak value of $\eta_{\rm col}\eta_{\rm dep} = 8\%$ is obtained at an optimal laser spot size of $w_{\rm L} = 10$ μm, however, such a small spot size is technically challenging for ignition-scale laser facilities. Also, the energy required for ignition is 18 kJ according to Atzeni's ignition scaling model [48], implying that 110% of $\eta_{\rm REB}$ is necessary to achieve ignition, which is unfeasible. Conversely, $\eta_{\rm col}$ decreased more gradually when the laser spot was expanded with the REB collimation method in this study. $\eta_{\rm col}\eta_{\rm dep}$ decreased from around $w_{\rm L} = 100$ μm because the REs gave energy to the background plasma and were unable to deliver energy to the fuel core. The maximum $\eta_{\rm col}\eta_{\rm dep}$ of 31% was achieved at the optimal spot size, $w_{\rm L} =$ 90 μm, which is possible in current large laser facilities. To realize ignition, an attainable $\eta_{\rm REB}$ of 29% is required [49,50].

ACKNOWLEDGMENTS

The authors thank the technical support staff at Osaka University for assistance with laser operation, target fabrication, plasma diagnostics, and computer simulation. This work was partly achieved through the use of large-scale computer systems at the Cybermedia Center at Osaka University. This work was supported by the Joint Usage/Research Center program of the Institute of Laser Engineering (ILE) at Osaka University (2023A1-017FUJIOKA); the Collaboration Research Program between the National Institute for Fusion Science and ILE (2020NIFS12KUGK057) and Grants-in-Aid for Scientific Research (No. 23K03360, No. 22H00118, No. 22H01205, No. 22H01206, No. 22K03567, No. 21H04454, No. 20H00140, No. 20H01886, No. 17K05728, and No. 16H02245), "Power Laser DX Platform" as research equipment shared in the Ministry of Education, Culture, Sports, Science and Technology Project for promoting public utilization of advanced research infrastructure (Program for advanced research equipment platforms, Grant No. JPMXS0450300021); the Japan Society for the Promotion of Science Core-to-Core Program (Grant No. JPJSCCA20230003); and the collaboration research between the ILE and EX-Fusion and that between the ILE and Blue Laser Fusion Inc.. R.T. and J.D. are partially supported by the QLEAR fellowship program of Osaka University.

APPENDIX A: PARTICLE-IN-CELL SIMULATION

Collisionless two-dimensional (x-y) particle-in-cell simulations were performed under the pre-plasma-free condition. The laser propagates in $+x$ direction and is polarized in the y direction. The laser intensity, wavelength, laser beam waist of $1/e$, and pulse duration are $I = 4 \times 10^{18}/\lambda_0^2$ (W cm^{-2} μm^{-2}), λ_0 (μm), $50\lambda_0$, and 0.8 λ_0 ps, respectively. Both taper and plane plasmas consist of fully ionized carbon and hydrogen, and its electron density is $70n_{\rm c}$, here $n_c = 4\pi^2 m_e/\mu_0 e^2\lambda_0^2$ is the critical density. The cone tip size and cone angle are $30\lambda_0$ and 90°, respectively. The cell size is $x = y = \lambda_0/64$ and number of electrons per cell is 100. Electrons whose kinetic energy is more than 100 keV at laser peak timing are illustrated in Fig. 1.

APPENDIX B: REFLECTIVITY OF PLASMA MIRROR

The LFEX laser consists of four beams, referred to as H1, H2, H3, and H4. The on-target energies are calculated by multiplying the beam energies ($E_{\rm H1}$, $E_{\rm H2}$, $E_{\rm H3}$, and $E_{\rm H4}$), which are measured before the beams enter the pulse compressor, and the measured energy transmittance of the pulse

TABLE I. Results of drag heating efficiency. The shaded cells show results obtained with an external magnetic field.

Contrast	Shot ID	Heating timing [ns]	Heating energy on the targets [J]	Pulse duration [ps]	Mean REB energy [MeV]	measured Cu-K_α number [10^{11} Photon/str]	Drag heating efficiency [%]
High	43801	0.20 ± 0.03	380 ± 60	2.6	1.3 ± 0.1	2.4 ± 0.5	4.4 ± 0.8
High	43789	0.28 ± 0.03	320 ± 50	2.8	0.64 ± 0.01	1.8 ± 0.4	4.3 ± 0.8
High	43798	0.30 ± 0.03	360 ± 60	1.5	2.5 ± 0.3	2.8 ± 0.6	4.9 ± 0.9
High	43790	0.36 ± 0.03	320 ± 50	2.1	0.91 ± 0.06	2.3 ± 0.5	5.4 ± 1.0
High	43780	0.53 ± 0.03	410 ± 70	1.3	1.4 ± 0.6	2.6 ± 0.5	4.6 ± 0.9
High	43782	0.53 ± 0.03	350 ± 60	2.7	0.62 ± 0.05	3.0 ± 0.6	6.6 ± 1.2
High	43802	0.57 ± 0.03	360 ± 60	2.1	1.0 ± 0.1	2.2 ± 0.4	4.8 ± 0.9
High	43783	0.58 ± 0.03	390 ± 70	2.8	0.68 ± 0.07	3.0 ± 0.6	5.9 ± 1.1
High	43797	0.71 ± 0.03	350 ± 60	2.3	0.72 ± 0.02	2.5 ± 0.5	5.6 ± 1.0
High	43788	0.79 ± 0.03	370 ± 60	2.6	0.87 ± 0.05	2.4 ± 0.5	5.3 ± 0.9
High	43792	0.90 ± 0.03	420 ± 70	2.0	0.78 ± 0.02	3.4 ± 0.7	6.4 ± 1.2
Medium	40549	0.37	670	1.9	3.6 ± 0.1	2.2 ± 0.4	2.1 ± 0.4
Medium	40547	0.38	1100	1.9	3.6 ± 0.01	3.9 ± 0.8	2.3 ± 0.5
Medium	40558	0.41	1520	2.1	20 ± 1	4.2 ± 0.8	1.7 ± 0.3
Medium	40545	0.42	900	1.6	6.9 ± 0.6	1.6 ± 0.3	1.1 ± 0.2
Medium	40556	0.61	1020	1.8	2.4 ± 0.1	2.9 ± 0.6	1.9 ± 0.4
Medium	40541	0.65	680	2.2	4.0 ± 0.01	1.6 ± 0.3	1.5 ± 0.3
Medium	40543	0.72	630	1.8	4.2 ± 0.2	2.7 ± 0.5	2.8 ± 0.6
Low	43465	0.46 ± 0.03	690	1.6	9.4 ± 1.1	0.98 ± 0.20	0.85 ± 0.09
Low	43473	0.40 ± 0.03	950	5.6 ± 1.3	3.5 ± 0.4	0.62 ± 0.12	0.42 ± 0.04
Low	43476	0.40 ± 0.03	1060	7.9 ± 1.3	8.1 ± 2.3	1.2 ± 0.23	0.66 ± 0.07
Low	43482	0.56 ± 0.03	1200	12.3 ± 1.3	2.2 ± 0.1	0.44 ± 0.09	0.25 ± 0.03

compressor ($\eta_{H1} = 0.73$, $\eta_{H2} = 0.62$, $\eta_{H3} = 0.58$, and $\eta_{H4} = 0.63$). The pulse durations are t_{H1}, t_{H2}, t_{H3}, and t_{H4}, and the radius is $r_L = 50$ μm. The laser energy on the target E_{target} without the PM was evaluated using the following equation:

$$E_{target} = \eta_{H1}E_{H1} + \eta_{H2}E_{H2} + \eta_{H3}E_{H3} + \eta_{H4}E_{H4}. \quad \text{(B1)}$$

The reflectance of the PM depends on the fluence F (J/cm^2) on the PM. The fitting curve for $F > 30$ J/cm^2 within a 95% confidence interval obtained from a previous work [35] is

$$R(F) = 0.52 \pm 0.11 - (2.0 \pm 2.1) \times 10^{-2} \times \ln F. \quad \text{(B2)}$$

The areas of the four beams on the PM were measured from the burn patterns of the beams on the PM after the laser shot. The fluences F_{H1}, F_{H2}, F_{H3}, and F_{H4} on the PM were calculated using the measured areas and energies. The laser energy on the target $E_{target,\ PM}$ with the PM was evaluated using the following equation:

$$E_{target,\ PM} = R(F_{H1})\eta_{H1}E_{H1} + R(F_{H2})\eta_{H2}E_{H2} + R(F_{H3})\eta_{H3}E_{H3} + R(F_{H4})\eta_{H4}E_{H4}. \quad \text{(B3)}$$

The laser energies on target for all shots are described in Table I.

APPENDIX C: DIAGNOSTICS

A calibrated Bragg crystal spectrometer was used for measuring the absolute photon numbers of Cu-K_α lines (Table I). The Bragg crystal in the spectrometer was a flat highly oriented pyrolytic graphite (HOPG) with an energy resolution of 17.9 eV. The absolute reflectance of the highly oriented pyrolytic graphite was $(5.0 \pm 1.0) \times 10^{-8}$ str within a 95% confidence interval, including the solid angle and assuming emission from a point source. The Bragg crystal spectrometer was installed at an angle of 43° from the axis of the heating laser. The imaging plate, which converted a signal to a number of photons based on a previous study [51], was used as the detector. The x rays entered the detector after passing through 500-μm-thick Be and 50-μm-thick polystyrene to protect the crystal from debris and reduce noise and background in the spectrum. The absolute photon number of the Cu-K_α lines was integrated from 8.0 to 8.1 keV in the measured spectrum to ignore shifted K_α signals in this study. In several shots, the plasma directly heated at the cone tip becomes highly ionized, causing a shift in the Cu-K_α lines. Because it is challenging to distinguish between drag heating and diffusive heating in these instances, this study disregards these heating effects. The background is defined as the average in the range 7.9–7.99 keV. The x-ray spectra normalized by the heating laser energy are shown in Fig. 7. The absolute photon number of the Cu-K_α lines per unit of heating laser energy increased with increasing laser contrast. The spectra in this figure do not account for x-ray absorption by the plasma.

An energy-calibrated electron spectrometer [52] was used for measuring the energy distribution of the REB. The electron spectrometer captured electrons passing through the collimator and measured the energy distribution for electrons that were dispersed by a magnetic field. The field of view of the electron spectrometer covered the entire plasma. The electron spectrometer was installed at 20.9° with respect to the heating laser axis. The energy distribution of the REB was fitted with the following two-temperature Maxwell-Boltzmann

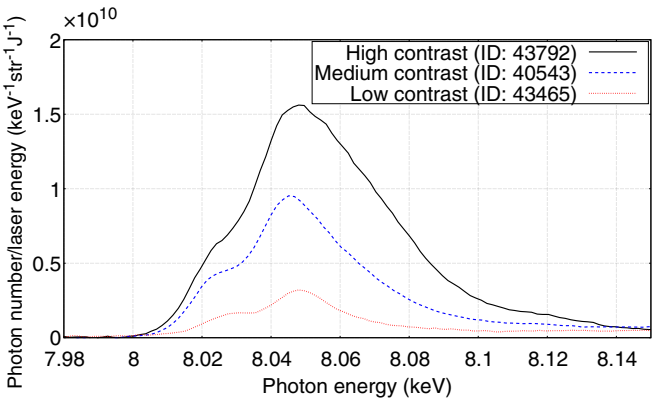

FIG. 7. The black, blue dashed, and red dotted curves represent the Cu-K_α lines normalized by laser energy in the high-, medium-, and low-contrast cases, respectively. The opacity of the plasma was not considered. The background was uniformly subtracted based on the average from 7.9 to 7.99 keV. The absolute photon number of the Cu-K_α lines was accumulated from 8.0 to 8.1 keV.

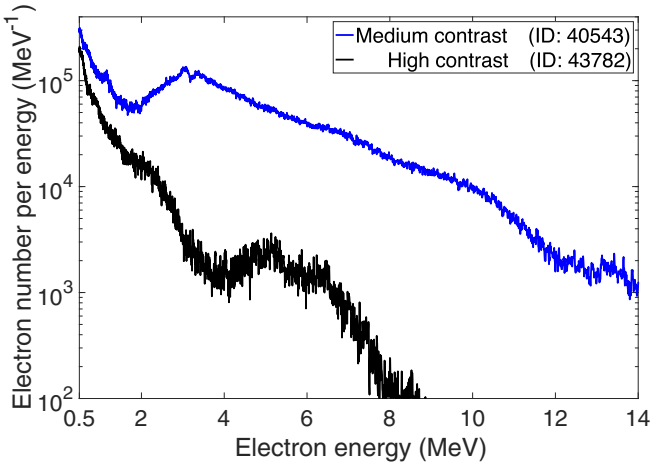

FIG. 8. Energy distributions of REs for medium- and high-contrast cases (blue and black curves, respectively).

distribution:

$$f(E) = A\exp(-E/T_{\mathrm{REB1}}) + (1-A)\exp(-E/T_{\mathrm{REB2}}), \quad \text{(C1)}$$

where $0 < A \leqslant 1$ is the intercept and $T_{\mathrm{REB1}} < T_{\mathrm{REB2}}$ are the slope temperatures (Table II). The mean kinetic energy of the REB presented in this paper was obtained using Eq. (C1). Figure 8 shows the energy distributions of REs.

A spherical crystal imager with a quartz (2131) crystal, whose radius of curvature was 200 mm, was used for measuring the monochromatic images of the Cu-K_α lines. The magnification, spatial resolution, and energy bandwidth were 16.9, 13 μm (FWHM), and 5 eV (FWHM), respectively. The x-ray image was measured at 2.7°, which is twice the Bragg angle, from the vertical axis of the heating laser.

An x-ray streak camera measured the incident timing between the compression laser and the heating laser. The timing was defined as the interval between the peak emission of the fuel plasma and the peak of the hard x rays generated by the heating laser.

TABLE II. Measured parameters for REB. The shaded cells show results obtained with an external magnetic field.

Contrast	Shot ID	Laser Intensity 10^{18} (W/cm^2)	A	T_{REB1} (MeV)	T_{REB1} (MeV)	Mean REB energy (MeV)	Correlation factor 10^{11} (J photons^{-1} sr^{-1})
High	43801	1.8 ± 0.3	1.0	1.1 ± 0.1	—	1.3 ± 0.1	4.7
High	43789	1.5 ± 0.2	1.0	0.54 ± 0.01	—	0.64 ± 0.01	5.2
High	43798	3.1 ± 0.5	1.0	2.4 ± 0.3	—	2.5 ± 0.3	4.4
High	43790	1.9 ± 0.3	0.73 ± 0.06	0.25 ± 0.03	1.0 ± 0.2	0.91 ± 0.06	5.0
High	43780	4.1 ± 0.7	0.80 ± 0.07	0.39 ± 0.07	1.8 ± 0.6	1.4 ± 0.6	4.8
High	43782	1.6 ± 0.3	1.0	0.51 ± 0.05	—	0.62 ± 0.05	5.2
High	43802	2.2 ± 0.4	1.0	0.89 ± 0.04	—	1.0 ± 0.1	4.9
High	43783	1.8 ± 0.3	1.0	0.57 ± 0.06	—	0.68 ± 0.07	5.1
High	43797	1.9 ± 0.3	1.0	0.60 ± 0.02	—	0.72 ± 0.02	5.1
High	43788	1.8 ± 0.3	0.90 ± 0.01	0.20 ± 0.01	1.3 ± 0.01	0.87 ± 0.05	5.2
High	43792	2.6 ± 0.4	1.0	0.66 ± 0.02	—	0.78 ± 0.02	5.0
Medium	40549	4.6 ± 0.2	1.0	3.4 ± 0.1	—	3.6 ± 0.1	4.3
Medium	40547	7.4 ± 0.3	1.0	3.4 ± 0.1	—	3.6 ± 0.1	4.3
Medium	40558	9.4 ± 0.5	0.96 ± 0.01	2.7 ± 0.1	43 ± 0.6	20 ± 1	3.9
Medium	40545	7.1 ± 0.4	1.0	6.7 ± 0.6	—	6.9 ± 0.6	4.0
Medium	40556	7.2 ± 0.4	1.0	2.2 ± 0.1	—	2.4 ± 0.1	4.5
Medium	40541	4.0 ± 0.2	1.0	3.8 ± 0.1	—	4.0 ± 0.01	4.2
Medium	40543	4.5 ± 0.2	1.0	3.9 ± 0.2	—	4.2 ± 0.2	4.2
Low	43465	5.4 ± 0.3	0.53 ± 0.36	0.79 ± 0.75	9.8 ± 0.4	9.4 ± 1.1	4.0
Low	43473	2.1 ± 0.5	1.0	3.3 ± 0.4	—	3.5 ± 0.4	4.3
Low	43476	1.7 ± 0.3	0.74 ± 0.02	0.62 ± 0.07	9.0 ± 2.3	8.1 ± 2.3	4.0
Low	43482	1.2 ± 0.2	1.0	2.0 ± 0.1	—	2.2 ± 0.1	4.5

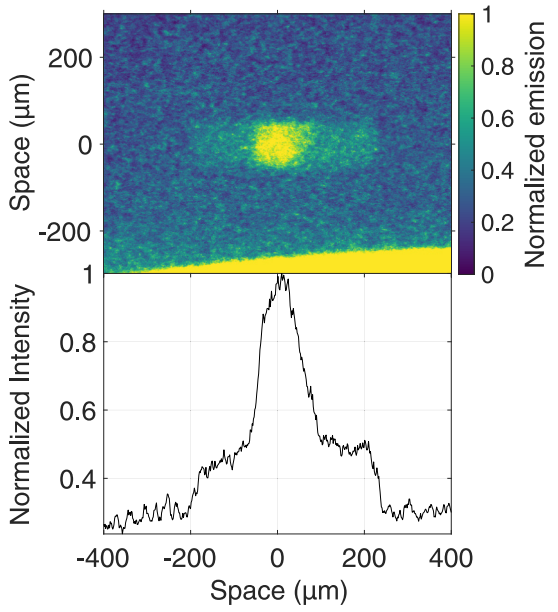

FIG. 9. Raw data of Cu-K_α emission image. The image was taken by the spherical crystal imager. The cone was placed at the bottom in this figure. The profile was taken over entire region of the tracer target. The region used for analysis Fig. 3 is obtained by folding the rectangular region about its center and then averaging.

APPENDIX D: REB PROPAGATION MEASUREMENT

The two-dimensional emission density cross section of the Cu-K_α lines derived from the Cu-K_α emission image under the assumption of cylindrical symmetry along the heating laser axis is shown in Fig. 3. Figure 9 shows the raw data of the Cu-K_α emission image. The cone was attached to the bottom side of the figure. The whole tracer target produced emissions due to the electrons coming from the cone. The emission profile was taken from the whole tracer region. The x-ray mass attenuation coefficient factor $\mu = 9.1\ \mathrm{cm}^2/\mathrm{g}$ at 8.048 keV with an electron temperature of 0.1 eV was calculated using PROPACEOS [53]. The emission density cross section was corrected by the absolute photon number of the Cu-K_α lines measured with a calibrated x-ray spectrometer.

APPENDIX E: DERIVATION OF CORRELATION FACTOR

The correlation factor C (Table II) between the deposited energy and the absolute photon number for the Cu-K_α lines was calculated using a one-dimensional model. Electrons propagate in the plasma and lose energy, which changes the energy distribution function. The plasma mass density in this model was assumed to be constant at $\bar{\rho} = 6.8\ \mathrm{g/cm}^3$ with an areal density $\rho L = \int \rho(x)dx$ of $0.14\ \mathrm{g/cm}^2$, as measured by the spherical crystal imager [Fig. 4(b)]. Solodov's model [40] was used for the plasma stopping power $S(E)$. The energy distribution $f(E, x)$ of the REB propagating through the plasma, which accounts for the energy deposition, is given by

$$f(E, x) = f[g(E, x), 0]\left|\frac{d}{dE}g(E, x)\right|, \tag{E1}$$

$$g(E, x) = E + \int_0^x S[g(E, t)]dt, \tag{E2}$$

where E is the kinetic energy and x is the space along ρL. The initial energy distribution $f(E, 0)$ for the REB is assumed to be the same as that measured by the electron spectrometer. The validity of this assumption has been previously confirmed [54]. Both Davies' model [39] and Hombourger's model [38] were used for the electron-impact K-shell ionization cross-section model $\sigma_{K_\alpha}(E)$. The average correlation factor calculated from each cross-section model was used to determine the heating efficiency. The correlation factor was calculated as follows:

$$C = \frac{\int_0^{1\,\mathrm{GeV}} v(E)E[f(E, 0) - f(E, L)]dE}{\int_0^L \int_{10\,\mathrm{keV}}^{1\,\mathrm{GeV}} v(E)f(E, x)n_{\mathrm{Cu}}\sigma_{K_\alpha}(E)/4\pi dEdx}, \tag{E3}$$

where $L = \rho L/\bar{\rho}$ is the size of the plasma, $v(E)$ is the velocity of the electrons, and n_{Cu} is the number density of Cu atoms. Furthermore, η_{dep} was calculated as

$$\eta_{\mathrm{dep}} = \frac{\int_0^{1\,\mathrm{GeV}} v(E)E[f(E, 0) - f(E, L)]dE}{\int_0^{1\,\mathrm{GeV}} v(E)Ef(E, 0)dE}. \tag{E4}$$

[1] A. B. Zylstra *et al.*, Burning plasma achieved in inertial fusion, Nature (London) **601**, 542 (2022).

[2] A. L. Kritcher *et al.*, Design of inertial fusion implosions reaching the burning plasma regime, Nat. Phys. **18**, 251 (2022).

[3] H. Abu-Shawareb *et al.*, Lawson criterion for ignition exceeded in an inertial fusion experiment, Phys. Rev. Lett. **129**, 075001 (2022).

[4] H. Abu-Shawareb *et al.*, Achievement of target gain larger than unity in an inertial fusion experiment, Phys. Rev. Lett. **132**, 065102 (2024).

[5] S. E. Bodner, Critical elements of high gain laser fusion, J. Fusion Energy **1**, 221 (1981).

[6] M. Tabak *et al.*, Ignition and high gain with ultrapowerful lasers, Phys. Plasmas **1**, 1626 (1994).

[7] A. J. Kemp, Y. Sentoku, V. Sotnikov, and S. C. Wilks, Collisional relaxation of superthermal electrons generated by relativistic laser pulses in dense plasma, Phys. Rev. Lett. **97**, 235001 (2006).

[8] A. Debayle, J. J. Honrubia, E. d'Humières, and V. T. Tikhonchuk, Divergence of laser-driven relativistic electron beams, Phys. Rev. E **82**, 036405 (2010).

[9] J. C. Adam, A. Héron, and G. Laval, Dispersion and transport of energetic particles due to the interaction of intense laser pulses with overdense plasmas, Phys. Rev. Lett. **97**, 205006 (2006).

[10] J. S. Green *et al.*, Effect of laser intensity on fast-electron-beam divergence in solid-density plasmas, Phys. Rev. Lett. **100**, 015003 (2008).

[11] F. V. Hartemann, S. N. Fochs, G. P. LeSage, N. C. Luhmann, J. Woodworth, M. D. Perry, Y. J. Chen, and A. K. Kerman,

Nonlinear ponderomotive scattering of relativistic electrons by an intense laser field at focus, Phys. Rev. E **51**, 4833 (1995).
[12] N. Kumar, V. K. Tripathi, and B. K. Sawhney, Filamentation of a relativistic short pulse laser in a plasma, Phys. Scr. **73**, 659 (2006).
[13] A. P. L. Robinson, A. V. Arefiev, and D. Neely, Generating "superponderomotive" electrons due to a non-wake-field interaction between a laser pulse and a longitudinal electric field, Phys. Rev. Lett. **111**, 065002 (2013).
[14] K. Weichman, A. P. L. Robinson, F. N. Beg, and A. V. Arefiev, Laser reflection as a catalyst for direct laser acceleration in multipicosecond laser-plasma interaction, Phys. Plasmas **27**, 013106 (2020).
[15] A. J. Kemp, Y. Sentoku, and M. Tabak, Hot-electron energy coupling in ultraintense laser-matter interaction, Phys. Rev. E **79**, 066406 (2009).
[16] A. Sorokovikova, A. V. Arefiev, C. McGuffey, B. Qiao, A. P. L. Robinson, M. S. Wei, H. S. McLean, and F. N. Beg, Generation of superponderomotive electrons in multipicosecond interactions of kilojoule laser beams with solid-density plasmas, Phys. Rev. Lett. **116**, 155001 (2016).
[17] S. Atzeni and M. Tabak, Overview of ignition conditions and gain curves for the fast ignitor, Plasma Phys. Controlled Fusion **47**, B769 (2005).
[18] S. Kojima *et al.*, Electromagnetic field growth triggering superponderomotive electron acceleration during multi-picosecond laser-plasma interaction, Commun. Phys. **2**, 99 (2019).
[19] G. J. Williams, A. Link, M. Sherlock, D. A. Alessi, M. Bowers, A. Conder, P. DiNicola, G. Fiksel, F. Fiuza, M. Hamamoto, M. R. Hermann *et al.*, Production of relativistic electrons at subrelativistic laser intensities, Phys. Rev. E **101**, 031201(R) (2020).
[20] P. A. Norreys *et al.*, Experimental studies of the advanced fast ignitor scheme, Phys. Plasmas **7**, 3721 (2000).
[21] R. Kodama *et al.*, Fast heating of ultrahigh-density plasma as a step towards laser fusion ignition, Nature (London) **412**, 798 (2001).
[22] S. D. Baton *et al.*, Inhibition of fast electron energy deposition due to preplasma filling of cone-attached targets, Phys. Plasmas **15**, 042706 (2008).
[23] H. Cai *et al.*, Prepulse effects on the generation of high energy electrons in fast ignition scheme, Phys. Plasmas **17**, 023106 (2010).
[24] A. G. MacPhee *et al.*, Limitation on prepulse level for cone-guided fast-ignition inertial confinement fusion, Phys. Rev. Lett. **104**, 055002 (2010).
[25] T. Yabuuchi *et al.*, Transport study of intense-laser-produced fast electrons in solid targets with a preplasma created by a long pulse laser, Phys. Plasmas **17**, 060704 (2010).
[26] T. Ma *et al.*, Hot electron temperature and coupling efficiency scaling with prepulse for cone-guided fast ignition, Phys. Rev. Lett. **108**, 115004 (2012).
[27] D. P. Higginson *et al.*, High-contrast laser acceleration of relativistic electrons in solid cone-wire targets, Phys. Rev. E **92**, 063112 (2015).
[28] X. Vaisseau *et al.*, Collimated propagation of fast electron beams accelerated by High-Contrast laser pulses in highly resistive shocked carbon, Phys. Rev. Lett. **118**, 205001 (2017).
[29] J. Derouillat *et al.*, SMILEI : A collaborative, open-source, multi-purpose particle-in-cell code for plasma simulation, Comput. Phys. Commun. **222**, 351 (2018).
[30] H. C. Kapteyn, M. M. Murnane, A. Szoke, and R. W. Falcone, Prepulse energy suppression for high-energy ultrashort pulses using self-induced plasma shuttering, Opt. Lett. **16**, 490 (1991).
[31] S. Backus *et al.*, Prepulse suppression for high-energy ultrashort pulses using self-induced plasma shuttering from a fluid target, Opt. Lett. **18**, 134 (1993).
[32] D. M. Gold, Direct measurement of prepulse suppression by use of a plasma shutter, Opt. Lett. **19**, 2006 (1994).
[33] C. Ziener *et al.*, Specular reflectivity of plasma mirrors as a function of intensity, pulse duration, and angle of incidence, J. Appl. Phys. **93**, 768 (2002).
[34] G. Doumy, F. Quere, O. Gobert, M. Perdrix, P. Martin, P. Audebert, J. C. Gauthier, J. P. Geindre, and T. Wittmann, Complete characterization of a plasma mirror for the production of high-contrast ultraintense laser pulses, Phys. Rev. E **69**, 026402 (2004).
[35] Y. Arikawa *et al.*, Ultrahigh-contrast kilojoule-class petawatt lfex laser using a plasma mirror, Appl. Opt. **55**, 6850 (2016).
[36] H. Li *et al.*, Enhanced relativistic electron beams intensity with self-generated resistive magnetic field, High Energy Density Phys. **36**, 100773 (2020).
[37] Y. Iwasa *et al.*, Cu-oleate microspheres fabricated by emulsion method as novel targets for fast ignition laser fusion experiments, Fusion Eng. Des. **125**, 89 (2017).
[38] C. Hombourger, An empirical expression for K-shell ionization cross section by electron impact, J. Phys. B: At. Mol. Opt. Phys. **31**, 3693 (1998).
[39] J. R. Davies, R. Betti, P. M. Nilson, and A. A. Solodov, Copper K-shell emission cross sections for laser–solid experiments, Phys. Plasmas **20**, 083118 (2013).
[40] A. A. Solodov and R. Betti, Stopping power and range of energetic electrons in dense plasmas of fast-ignition fusion targets, Phys. Plasmas **15**, 042707 (2008).
[41] L. C. Jarrott *et al.*, Visualizing fast electron energy transport into laser-compressed high-density fast-ignition targets, Nat. Phys. **12**, 499 (2016).
[42] S. Sakata *et al.*, Magnetized fast isochoric laser heating for efficient creation of ultra-high-energy-density states, Nat. Commun. **9**, 3937 (2018).
[43] H. Daido, F. Miki, K. Mima, M. Fujita, K. Sawai, H. Fujita, Y. Kitagawa, S. Nakai, and C. Yamanaka, Generation of a strong magnetic field by an intense CO_2 laser pulse, Phys. Rev. Lett. **56**, 846 (1986).
[44] K. F. Law *et al.*, Direct measurement of kilo-tesla level magnetic field generated with laser-driven capacitor-coil target by proton deflectometry, Appl. Phys. Lett. **108**, 091104 (2016).
[45] M. Bailly-Grandvaux *et al.*, Guiding of relativistic electron beams in dense matter by laser-driven magnetostatic fields, Nat. Commun. **9**, 102 (2018).
[46] H. Morita, T. Ogitsu, F. R. Graziani, and S. Fujioka, Advanced analysis of laser-driven pulsed magnetic diffusion based on quantum molecular dynamics simulation, Matter Radiat. Extremes **6**, 065901 (2021).
[47] R. J. Gray *et al.*, Laser pulse propagation and enhanced energy coupling to fast electrons in dense plasma gradients, New J. Phys. **16**, 113075 (2014).

[48] S. Atzeni, Inertial fusion fast ignitor: Igniting pulse parameter window vs the penetration depth of the heating particles and the density of the precompressed fuel, Phys. Plasmas **6**, 3316 (1999).

[49] R. Town *et al.*, Simulations of electron transport for fast ignition using LSP, Nucl. Instrum. Methods Phys. Res. Sect. A **544**, 61 (2005).

[50] J. R. Davies, Laser absorption by overdense plasmas in the relativistic regime, Plasma Phys. Controlled Fusion **51**, 014006 (2008).

[51] A. L. Meadowcroft, C. D. Bentley, and E. N. Stott, Evaluation of the sensitivity and fading characteristics of an image plate system for x-ray diagnostics, Rev. Sci. Instrum. **79**, 113102 (2008).

[52] T. Ozaki *et al.*, An electron/ion spectrometer with the ability of low energy electron measurement for fast ignition experiments, Rev. Sci. Instrum. **85**, 11E113 (2014).

[53] J. MacFarlane, I. Golovkin, and P. Woodruff, HELIOS-CR A 1-D radiation-magnetohydrodynamics code with inline atomic kinetics modeling, J. Quant. Spectrosc. Radiat. Transfer **99**, 381 (2006).

[54] S. Fujioka *et al.*, Heating efficiency evaluation with mimicking plasma conditions of integrated fast-ignition experiment, Phys. Rev. E **91**, 063102 (2015).